PHYSICAL REVIEW B **107**, 054306 (2023)

Editors' Suggestion

Surface dynamics of graphite probed by soft x-ray linear dichroism in Auger-emission yield

G. Schiwietz,[*] T. Kachel, R. Mitzner, and K. Holldack
Helmholtz-Zentrum Berlin für Materialien und Energie GmbH, Albert-Einstein-Str. 15, 12489, Berlin, Germany

(Received 13 August 2022; revised 18 December 2022; accepted 18 January 2023; published 13 February 2023)

Time-resolved near-edge x-ray absorption with Auger-electron detection is employed as a surface-sensitive probe to study the dynamics of surface atomic motion in graphite upon laser excitation. To this end, ultrafast changes in photoelectron spectra with a focus on carbon *KVV*-Auger intensities are used as probe in a pump-probe scheme with pulsed femtosecond near-infrared laser excitation of a highly oriented pyrolytic graphite (HOPG) sample. The dynamics of the HOPG surface excitation at the *K* edge appears as transient change in Auger yield. Since the directional bond character of carbon is reflected in linear dichroism of x-ray absorption, the transient angular variation of the $1s \to \pi$ transitions can be used to uncover the laser-induced dynamics of the atomic surface structure which shows a huge anisotropy upon usage of *s*- or *p*-polarized x-ray probe pulses, respectively.

DOI: 10.1103/PhysRevB.107.054306

I. INTRODUCTION

Graphitic materials as well as carbon atoms have been subjects of intense physics research for many decades. The connection between carbon and life sciences, its directional bond character, pronounced layer structures, the semimetallic band structure, and other properties of graphitic structures have inspired many research projects. Here we concentrate on time-resolved x-ray absorption spectroscopy of highly oriented pyrolytic graphite (HOPG) by detection of Auger electrons. This is one of the few methods that are element specific and surface sensitive. In carbon, inner-shell Auger electrons are induced by the decay of a *K*-shell vacancy due to electron-electron interactions in the valence bands (*KVV* decay). A detailed analysis of the electron-induced *KVV*-Auger spectra of graphite was published by Houston *et al.* [1], who took into account the band structure and effects of static and dynamic initial-state screening.

Graphite has a layer structure with large interlayer separation. Thus, it may be considered a quasi-2D solid. Several groups have performed band-structure determinations for graphite using different methods [2]; some of the models do even provide partial electronic density-of-states (eDOS) information [3,4]. The 2D character of graphite is related to σ-type electronic orbitals within the basal plane and π-type orbitals in the perpendicular direction. By changing the target-tilt angle and/or incident polarization direction of an x-ray beam, linear dichroism (difference in absorption between *p polarization*, parallel to the scattering plane, and *s polarization,* perpendicular to this plane) comes into play. For HOPG this results in strong angular dependencies for resonance intensities for *K*-shell excitation into unpopulated σ or π orbitals. Reason is the angular dependence of these resonances from 1s into the $p\sigma^*$ or $p\pi^*$ orbitals as given by the specific angular-momentum character of the corresponding transition-matrix elements [5,6]. A target-tilt method based on this effect was used for the peak identification in absorption spectra as well as for the determination of interlayer states [7] and, finally, a very sharp core-hole excitonic peak [8] was identified.

While the static angular-dependent near edge x-ray absorption (NEXAFS) in HOPG is a textbook example [5,6]; a short-time dynamics study of NEXAFS is the main subject of this paper. The valence-electron dynamics of solid carbon in the presence of a high degree of electronic excitation has been investigated with fast- [9], as well as with slow [10], highly charged ions. Many papers on laser-induced emission of electrons, visible light, and THz radiation are related to the hot-electron dynamics in graphite. For low photon energies, multiphoton photoemission (mPP) governs the electron emission for any solid. Specifically in graphite, thermionic photoemission due to intraband Auger thermalization (after 5 to 10 fs at moderate laser intensity [11,12]) of electrons excited into the interlayer band of σ symmetry [13] is the most likely electron-ejection mechanism. While all these studies are providing only electron-dynamics information, a direct structural response cannot be clearly extracted. Therefore, in this work we will use polarization-angle dependent time-resolved (tr)-NEXAFS of the Auger yield near the carbon-*K* edge in order to demonstrate and thereby indirectly investigate the *lattice* dynamics at the surface upon strong near-infrared femtosecond-laser excitation.

II. EXPERIMENTS AND BOUNDARY CONDITIONS

A. Setup and methods

Experimental tests have mainly been performed at the UE112_PGM-1 [14] and the final pump-probe measurements at the UE56/1 PGM x-ray beamline [15] of the BESSY II storage ring of the Helmholtz-Zentrum Berlin using x-ray energies between 280 and 450 eV. We have used our special

---

[*] schiwietz@helmholtz-berlin.de

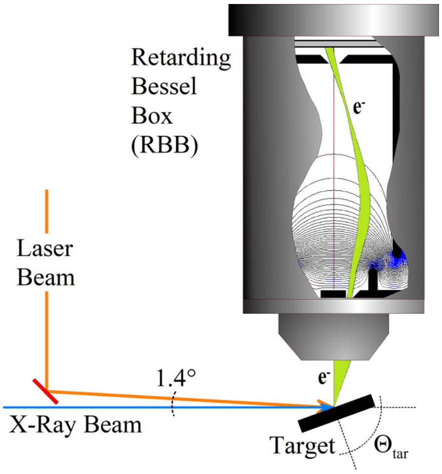

Schematic top view: NOT to scale

FIG. 1. Sketch of the experimental pump-probe arrangement using a quasicollinear overlap (1.4 °) between the laser beam (orange) and the X-ray beam (blue). Detection of electrons is performed by a high-throughput retarding Bessel box (RBB) spectrometer designed recently [16]. Corresponding electron optical simulation [16] is shown as equipotential lines (black and blue lines) as well a bundle of tracked electrons of equal kinetic energy (green).

electron-timing (ET) setup featuring residual-gas pressures of about 1.4×10^{-10} mbar and an electrostatic retarding Bessel-box (RBB) spectrometer [16] as depicted in Fig. 1 for sensitive Auger-electron measurements (related to a large detection solid angle and an optimized energy resolution) in the presence of huge mPP intensities as well as scattered laser photons. Low-energy electrons are blocked completely, because only electrons at energies above 90% of the nominal detection energy may pass the retardation potentials inside the RBB. Multiple mechanisms lead to an overall suppression of scattered laser photons by many orders of magnitude. These mechanisms operate electronically (via time-of-flight restrictions), geometrically (requiring a few large-angle scatterings inside the RBB) and physically (via the vanishing channel-plate detector efficiency below UV photon energies).

Details of such laser-pump x-ray-probe experiments with electron detection have been presented in previous papers [17]. Here, we present an ultrafast dynamic measurement of this type for *K*-shell excitation of a graphite surface. Similar as previous x-ray-diffraction measurements of coherent lattice vibrations in bismuth [18], the combination of polarization sensitivity and Auger-electron detection used in this work sheds light on fast-correlated lattice dynamics at surfaces employing Auger emission as an alternative probe channel for structural changes.

In short, we have performed a polarization-dependent NEXAFS measurement in the Auger channel employing the linear dichroism contrast of the $1s$ to π^* and σ^* resonances of HOPG. Setting the NEXAFS photon energies to the corresponding resonances, we pumped the sample by a collinear near-infrared laser beam at a wavelength of 800 nm and pulse lengths of 100 fs full width at half maximum (FWHM) at a repetition rate of 6 kHz. These nonresonant *s-polarized* [17] laser pulses involve a maximum pulse energy of 0.32 mJ corresponding to a maximum incident fluence of $\phi_{\text{in}} = 150\,\text{mJ/cm}^2$ (with an absorbed fraction of only $\phi_{abs} = 75\,\text{mJ/cm}^2$ at 45° incidence [19]), well below the graphite ablation threshold [20] of $185\,\text{mJ/cm}^2$ at normal incidence (absorbed fluence [19] of $\phi_{abs} = 123\,\text{mJ/cm}^2$). The x-ray spot projected onto the sample was about $200 \times 150\,\mu\text{m}^2$ (horizontal × vertical) using a 1200-lines per millimeter grating for photon-energy selection [15]. The polarization was selected by using the first harmonic from the Apple II undulator of 30 periods in planar-horizontal or planar-vertical mode, respectively [15]. The commercial HOPG target from Advanced Ceramics (serial No. 4357, 12 mm × 12 mm × 2 mm of 0.8° ± 0.2° mosaic spread) was cleaved in air and evacuated rapidly followed by annealing up to 850 K. Afterwards, no surface contaminations could be observed using photoelectron spectroscopy and Auger analysis. The detection of a very narrow exciton peak is consistent with a high surface quality of the HOPG sample, and with its small mosaic spread mentioned above. The experimental data presented further below have been mainly taken in a NEXAFS mode using Auger emission as probe channel for a constant electron-energy setting of the Bessel-box spectrometer [16] at the *KVV*-Auger peak maximum at about 260 eV. Auger electrons in graphite involve an inelastic mean-free-path of about 0.8 nm corresponding to dominant surface-layer sensitivity [21]. Total-electron-yield (TEY) spectra have been obtained during the Auger-electron measurements in a standard time-integrated mode (not sensitive to the laser excitation that is related to 0.001% of the photon pulses). TEY tests for two additional target-tilt angles are in accord with previously determined peak positions, intensities, and angular dependencies for TEY of HOPG [5,7,8].

B. Laser-induced temperatures

This section deals with the determination of the electron temperature T_e directly after the laser-excitation pulse and of the subsequent maximum HOPG lattice temperature T_{lattice}. Note that we apply two different irradiation geometries for the tr-NEXAFS experiments, the main subject of this work. Close to the excitation resonances, the integral Auger count rates must be kept below 400 kHz to ensure a linear detector response. For this case we use an incident angle Θ_{tar} of 45°. Far away from resonance conditions, we enhance the Auger count rate (by a factor of about 3) by taking advantage of the magnified excitation yield within the surface layers for near-grazing incidence irradiation (at 70° as shown in Fig. 1) further magnified by an enhanced Auger angular-emission fraction close to the surface normal.

Regarding the temperature determination, two different computations schemes are applied for characterizing the effect of individual laser shots on the target, considering the tr-NEXAFS irradiation conditions. The first method yields estimated maximum temperatures T_e and T_{lattice} by using the absorbed electronic energy density and well-accepted theoretical as well as experimental heat capacities for HOPG. The second method is based on a conversion of the measured pure laser-generated total electron-emission rates into maximum

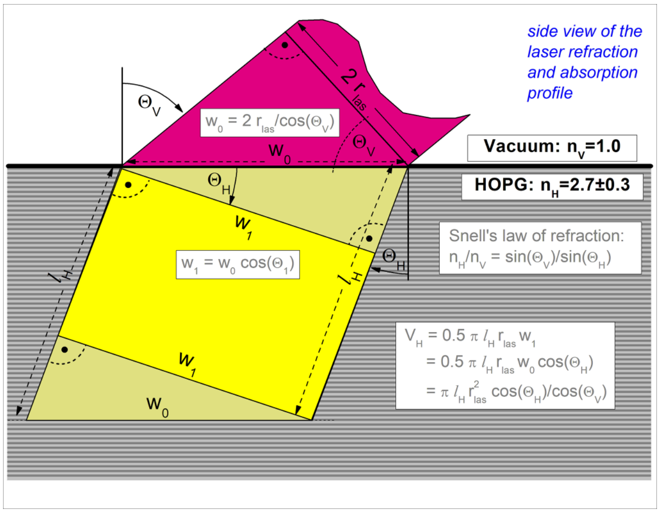

FIG. 2. Side view of the laser refraction and absorption profile. The index V in the plot indicates the vacuum half space above the surface and the index H indicates the bulk of the HOPG sample. Considering the refractive index $n_H = 2.7$ of HOPG [19], the absorption length l_H at $\lambda = 800$ nm (also taken from Ref. [19]) and Snell's law of refraction, the absorption volume V_H is computed under the assumption of sharp geometrical boundaries of the incident laser beam (of radius r_{las}) for the incident tilt angle Θ_V and the refracted beam at angle Θ_H. Numerical results are presented in Table I.

electron temperatures T_e before the electronic and/or global cooling phase.

Figure 2 displays the scheme for estimating the HOPG bulk volume V_H of the absorbed laser pulses, by considering a fixed absorption length and surface refraction along the formulas given in the figure. The refraction effect is often neglected but leads to a significant effect specifically at grazing-incidence irradiation at wavelengths related to a refractive index clearly above 1. Numerical results for the two irradiation geometries at 45° and 70° are given in Table I and also include the angle-dependent reflectivity of the s-polarized laser beam.

Figure 3 displays heat capacities $C(T)$ in the upper plot and related laser-induced volume-energy densities $dE/dV(T)$ in the lower plot as function of the temperature. These heat capacities include computed electronic heat capacities [22] [for the free-electron gas (FEG) and for graphitelike amorphous carbon (a-C)] scaled to the HOPG electron density as well as measured total values for different carbon structures taken from various literature sources [23–26]. The energy-density curves in the lower plot are directly derived from the corresponding heat capacities in the upper plot using the equation $\frac{dE}{dV}(T) = \int_0^T C(T')\, dT'$ as function of T. Provided the laser-induced absorbed energy density (the y axis) is known and diffusion of hot electrons may be neglected, the related lattice and electron temperatures are found on the x axis of Fig. 3(b). Note that ballistic electron transport in graphite may exceed a mean-free path of 1 μm at room temperature [27]. For the current conditions, we assume that fast electron diffusion might reduce the maximum energy density at the surface by a factor of 2 leading to temperature reductions of 25 to 30% [see Fig. 3(b)]. For a more detailed estimate, thermal-spike or two-temperature models could be invoked. Most of the current models, however, do not consider the graphite layer structure [22] or replace the electronic properties of graphite by simplified free-electron estimates [28,29].

The blue curve in the lower plot is extracted from the integral over the total heat capacity C_{total} as function of the maximum temperature $T_{\text{lattice}}^{\max}$, assuming no significant heat conduction into the sample and no radiation or electron cooling after a rapid equilibration of electron and lattice tem-

TABLE I. Primary and calculated laser-beam parameters related to Fig. 2 and the resulting limits for the lattice and electron temperatures. The pump laser delivers pulses at a wavelength λ_0 with a time duration of about $\Delta t = 100$ fs at a repetition rate of $f_{rep} = 6.032$ kHz. These pulses at a pulse energy E_{pulse} are incident on the sample at a tilt angle $\Theta_V = \Theta_{tar}$ with respect to the target-surface normal (see Figs. 1 and 2) and they are always s-polarized. For crystalline graphite and $\lambda_0 = 800$ nm, the refractive index is $n_H = 2.7 \pm 0.3$ and the absorption length is $l_H = 1/\alpha = (43 \pm 7)$ nm [19], equivalent to 64 graphite layers at normal incidence. The atomic volume density of HOPG and also the density of occupied $2p\pi$ electrons (corresponding to 1 electron per atom close to the Fermi level) is $dn/dV = 1.1335 \times 10^{20}$ atoms/mm^3.

Incident angle Θ_V	45°	70°	
Laser power P	0.94 W	1.96 W	
Incident energy E_{pulse}	0.156 mJ	0.325 mJ	$= P/f_{rep}$
Projected cross section A_{in}	(0.105 ± 0.015) mm^2	(0.216 ± 0.030) mm^2	$= A_{\text{las}}/\cos(\Theta_V)$
Incident fluence per pulse ϕ_{in}	149 mJ/cm^2	150 mJ/cm^2	$= E_{\text{pulse}}/A_{in}$
s-polarization reflectivity R_s	0.45 ± 0.04	0.67 ± 0.03	from Ref. [19]
Absorbed pulse fluence ϕ_{abs}	(82 ± 11) mJ/cm^2	(50 ± 7) mJ/cm^2	$= (1 - R_s)\,\phi_{in}$
Refracted angle Θ_H	15.2° ± 1.4°	20.4° ± 1.9°	see Fig. 2
Energy absorption volume V_H	4357 μm^3	8705 μm^3	$= l_H A_{in} \cos(\Theta_H)$; see Fig. 2
Volume energy density dE/dV	(19.7 ± 3.6) J/mm^3	(12.3 ± 2.5) J/mm^3	$= (1 - R_s)\,E_{\text{pulse}}/V_H$
Valence electronic energy $E_{2p\pi}$	$(1\,085 \pm 200)$ meV	(677 ± 140) meV	$= {}^{dE}/_{dV}/{}^{dn}/_{dV}$
Max. lattice temperature[a]	4 572 K [No. 2]	3 323 K [No. 1]	from Fig. 3
Max. electron temperature[b]	18 713 K [No. 5]	15 390 K [No. 4]	from Fig. 3
Peak electron temperature[c]	< 5560 K	< 5510 K	from Fig. 4

[a] Assumes prompt coupling to the lattice. No. 1 and No. 2 are related to the markers in Fig. 3.

[b] Assumes slow coupling to the lattice. No. 4 and No. 5 are related to the markers in Fig. 3.

[c] Derived from electron-emission yields for a hot-phase duration exceeding 50 fs.

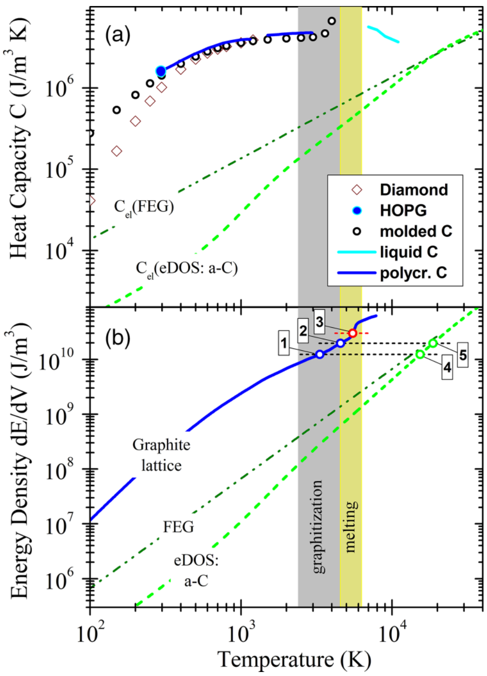

FIG. 3. Thermal properties of carbon as function of an equilibrium temperature T. The two green curves in the upper plot represent computed electronic heat capacities of the free-electron gas (FEG) and of graphitelike amorphous carbon scaled to the HOPG density, taken from a previous ultrashort-time investigation [22]. Other curves in the upper plot show the total heat capacity C_{total} of liquid and solid carbon types, by different research groups [23–26]. These results coincide at lattice temperatures above 500 K. The gray and yellow bars indicate temperature regions where soft carbon types are converted into graphite and where melting starts, taken from the three most recent experimental data [26]. The lower plot shows corresponding curves of the energy density as function of T as well as five markers that indicate thermal parameters that are important to our experiments (see text and Table I).

peratures. The blue circles marked [No. 1] and [No. 2] (see also Table I) stand for the maximum possible lattice temperatures at $\Theta_{tar} = 70^\circ$ (used for *s-polarized* x rays) and for 45° (used for *p-polarized* x rays), respectively. The computed temperature difference between the 45° measurement and the 70° data is mainly due to angle-dependent variations of the surface reflectivity (see Table I) for the *s-polarized* laser beam. The red circle marked [No. 3] displays the ablation threshold [20], corresponding to a volume-energy density of 30 J/mm^3 at $T_{\text{lattice}} = 5510$ K.

The green (dashed and dashed-dotted) curves in Fig. 3(b) display the relation between dE/dV and the maximum electron temperature $T_e^{\max}$ for a free-electron gas and for a graphitelike electronic band structure assuming short times after the laser pulse without significant coupling of electronic energy to the lattice. The green markers [No. 4] and [No. 5] relate to the same experimental conditions as the markers [No. 1] and [No. 2] but stand for the maximum possible *electron* temperatures ($T_e^{\max} = 15\,390$ and 18 713 K; see also Table I), respectively.

Figure 4 display estimates for the relation between electron temperature at the surface and electron emission yield per laser pulse, based on the Richardson formula [30,31] for thermionic emission. We describe the number of ejected target electrons per pulse N_e as a thermionic emission using a slightly modified Richardson equation:

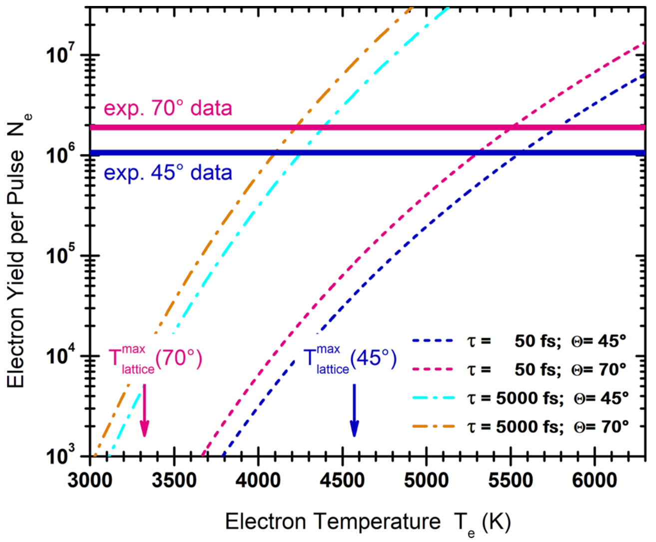

FIG. 4. Determination of the electron temperature from measured target-electron currents. Experimental electron-emission data corresponding to the two investigated cases are $N_e = 1.89 \times 10^6\ e^-$/pulse for the incident angle Θ_{tar} of 70° ($P = 1950$ mW) and $1.06 \times 10^6\ e^-$/pulse for $\Theta_{tar} = 45^\circ$ ($P = 925$ mW). Results of the Richardson equation for thermionic emission are shown for these two experimental conditions and for two extreme-cooling scenarios. These scenarios are an ultrafast cooling with $\tau = 50$ fs and alternatively very long HOPG electron-phonon equilibration times of $\tau = 5$ ps. Crossings of the horizontal solid lines representing the above experimental data and the Richardson curves (dashed lines) determine the effective electron temperature during time τ (see text).

$$\boldsymbol{N_e} = \boldsymbol{A_{in}} \cdot \boldsymbol{C_{mod}} \cdot \boldsymbol{\tau_e} \cdot \boldsymbol{T_e^2} \cdot \exp\left(-\frac{\boldsymbol{\phi_{eff}}}{\boldsymbol{k_B} \cdot \boldsymbol{T_e}}\right).$$

Here, $\boldsymbol{A_{in}}$ is the projected laser-beam cross section (see Table I), $\boldsymbol{C_{mod}} = 3.74 \times 10^{24}\ \mathrm{e^-/s/m^2/K^2}$ is an effective Richardson constant considering a 50% space-charge suppression [17,30], ϕ_{eff} is the work function of HOPG (***4.55* eV**) increased by a band-structure offset (***1.8* eV**) adjusted to the populated eDOS [22] of the semimetal, τ_e is the time duration at the elevated electron temperature $\boldsymbol{T_e}$. It is noted that the Richardson equation is often used at constant target temperature for the determination of work functions. As can be seen in Fig. 4, this formula yields an extremely steep increase of the ejected electron rate as a function of electron temperature (below 70 000 K, where the exponential function is far below its limiting value of 1). The time duration in the formula depends on the laser pulse length as well as on the efficiency of electron-cooling processes. $\boldsymbol{\tau_e}$ must be clearly above the carbon *KVV*-Auger decay time of 11 fs, where no significant coupling to the lattice has been observed [9,22]. Thus, the shortest duration to be considered is $\tau_e = 50$ fs, half the laser pulse length and as an upper limit we have chosen a typical slow electron-phonon relaxation time of a few picosecond. One can see that the steepness of the curves compresses this time variation of a factor of 100 down to an electron-temperature variation of only 25%. The computed electron yield is equal to the experimental one at the crossing of a steep thermionic emission curve and the corresponding experimental value (horizontal line). In this way, one may extract electronic peak temperatures of $T_e^{\text{peak}} \cong 4240$ K assuming $\tau_{\mathbf{e}} = 5000$ fs and $T_e^{\text{peak}} \cong 5540$ K assuming $\tau_{\mathbf{e}} = 50$ fs. The last rows of Table I summarize the parameters and temperature results from Figs. 2, 3, and 4 used to characterize the pump-probe experiments described further below.

Using consistency considerations, one may further improve the accuracy of the temperature determination and derive an estimate for the electron-phonon coupling time. The maximum electron temperature must exceed the maximum lattice temperature, because the laser energy is initially transferred to the electron system and only afterwards dissipated to the lattice. The largest computed lattice temperature (from Figs. 2 and 3 and Table I) is shown by the blue arrow in Fig. 4. This consistency check would limit the acceptable time and temperature ranges only if fast electronic diffusion can be neglected. Otherwise, both arrows would shift to lower temperatures. However, if the green markers [No. 4] and [No. 5] for the electron temperature without electron-phonon coupling and without diffusion in Fig. 3 (>15 000 K) are considered, it follows that the electron-phonon coupling time should be close to the laser pulse length to restrict the (indirectly measured) electron temperature to about 5500 K. Thus, we assume a high-temperature duration of $\tau_{\mathbf{e}} = 50$ to 200 fs corresponding to electronic peak temperatures of about $T_e^{\text{peak}} = (5300 \pm 250)$ K and similar electron-phonon coupling times $\tau_{\mathbf{e\text{-}ph}}$. The expected range of $\tau_{\mathbf{e\text{-}ph}}$ is in reasonable agreement with the literature values of 250 fs [32,33], 180 fs [34], and about 100 fs [35] (at $\lambda = 800$ nm) for cooling via strongly coupled optical phonons at moderate to high laser-power density in HOPG. At very low pump power τ_e may exceed 1 ps [36]. It seems that the current literature data do not allow for a distinction between the importance of electron-phonon scattering related to the kinetic electron energy or cold melting [37] involving the potential energy of electronic holes. The fact that electron cooling seems to be faster at high laser-energy densities, however, points to an influence of nonlinear effects in the initial cooling phase.

III. RESULTS AND DISCUSSION

A. Static electron spectra and pump-probe alignment

Figure 5 displays two HOPG reference electron spectra in the electron-energy range of 0 to 470 eV for linearly polarized x-ray light at 450 eV and two polarization directions. The electron spectrometer was placed in the horizontal plane at 90 ° with respect to the incident x-ray beam. These experiments have been performed at an incident angle of $\Theta_{tar} = 45^\circ$ with respect to the target-surface normal for two linear polarization directions. The spectra are dominated by structures due to photoionization of the *K* shell (K-PI) and the valence band (*V*-PI) as well as a broader structure due to *KVV*-Auger transitions at about 260 eV. At the low-energy side, each of these three structures is accompanied by a smooth background due to individual electron-energy losses and by a superimposed peak due to collective plasmon energy losses ($\omega_{pl} = 25$ eV). Close to zero energy there is the sharp cascade peak incorporating the low-energy analog of individual electron-cascade processes.

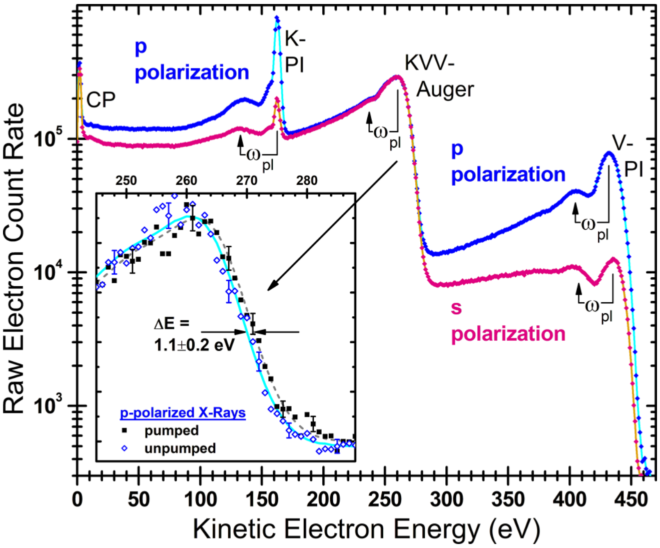

FIG. 5. Nonresonant wide-scan survey spectra of ejected electrons due to linearly polarized x-ray light on HOPG at an incident energy of 450 eV (electron-energy resolution $\Delta E/E = 3\%$, no laser excitation). The two spectra have been taken for *horizontal (in the scattering plane or p) and vertical (out-of-scattering-plane or s) polarization* directions. The missing linear dichroism of the Auger peak proves that the cross sections for excitation into final high-energy continuum states far above any resonance do not depend on the polarization direction. Inset: These data have been taken under similar conditions as the blue curve in the main plot, but with laser pulses on the target. The open blue diamond symbols show quasiunpumped electron signals that are gated with synchronous laser pulses arriving long after an x-ray pulse. The light-blue solid curve is derived from an intensity scaling of the corresponding ungated reference spectrum (as in the main plot) that has been measured simultaneously. Solid black symbols represent the pumped situation where the laser pulse hits the target slightly before an x-ray pulse. The scaled ungated reference spectrum had to be shifted by 1.1 eV towards higher energy (dashed gray curve) in order to fit the pump effect.

The Auger peak does not depend on the x-ray polarization direction because the nonresonant *K* ionization at high photon energies (450 eV) does not involve any preferential direction in the ionized carbon atom and the decaying 1*s* state leads to a constant (nearly spherical) Auger-electron production. This is different for photoionization. An electric-field vector in the electron-detection direction leads to a strong intensity enhancement in this case. This can directly be seen in Fig. 5, where the effect of *p* polarization (towards the electron-detection angle) is shown in the upper (blue) curve. For *s* polarization (the lower pink curve), primary electron emission occurs within the basal planes of HOPG, as follows for 1*s* and two 2*s* electrons directly from the atomic dipole-selection rules. Thus, subsequent scattering inside the bulk and surface is necessary for ejecting a fraction of these electrons also towards the spectrometer [38].

The inset in Fig. 5 shows the *KVV*-Auger peak of the same HOPG sample for *p*-polarized x-ray light at 450 eV using a linear count-rate scale. This plot serves as a check of the pump-probe alignment in time and space. It includes three different datasets and one fit. The symbols show two measurements (partly with statistical error bars) related to a specific bunch within the gap of the synchrotron fill pattern (the so-called camshaft bunch) accompanied by synchronized shots of the excitation laser at a laser power of 946 mW, at two different delays. Note that the production of the required pulse energy (up to nearly 0.4 mJ for the dynamics experiments discussed later) is not available at the synchrotron repetition rate of 1.25 MHz and the corresponding high average-absorbed power would lead to unwanted heating of the HOPG sample surface. Thus, we are using a constant laser-repetition frequency of 6 kHz throughout this work. Each Auger-electron signal was gated with the trigger of the actively synchronized laser such that direct detection of scattered photons is suppressed for a few nanoseconds and subsequent electron counts are accepted for the next 20 to 100 ns (dependent on the selected electron-energy range). Technically, this was done with standard NIM electronics modules involving mainly an amplifier, a constant fraction-signal discriminator, a digital delay generator, a time-to-amplitude converter for deriving time spectra, and a single-channel analyzer for selecting a specific timing condition. These gated pulses as well as the ungated pulses from the discriminator are sent to the data acquisition system together with other secondary data.

The blue diamond symbols in the inset show quasiunpumped electron signals, where laser pulses arrive long after an x-ray pulse (with a delay of 300 ps) and Auger electrons are far away from the surface when the slow electrons are generated by the femtosecond-laser pulse. The light-blue solid curve is derived from an intensity scaling of the corresponding ungated reference spectrum that has been measured simultaneously. This curve involves extremely low statistical errors, since it stems from continuous electron counting (as the blue curve in the main plot), with only one laser shot every 6×10^4 x-ray pulses. To within the error margins, the intensity scaling is consistent with the corresponding current ratio of all bunches vs the gated ones.

Gating the emitted Auger electrons with a laser pulse that is followed by an x-ray pulse after about 60 ps leads to the results displayed by the black square symbols denoted pumped in the inset. The underlying dashed-gray curve is an intensity-scaled curve, similar as the blue one. The gray curve, however, has been shifted towards higher energy by about 1.1 eV to fit the pumped data. This well-known space-charge shift is related to the large number of low-energy laser-generated electrons that accelerate the Auger electrons in the vicinity of the surface towards even higher energy [17]. The space-charge shift allows for an optimization of the spatial overlap of laser- and x-ray beam and it indicates a reasonable setting of the laser delay. The timescale calibration via this space-charge effect clearly exceeds the precision of our initial calibrations by detecting both beams with an avalanche photodiode. Before turning to the HOPG solid-state dynamics using pump-probe NEXAFS, static NEXAFS properties are presented in the next section.

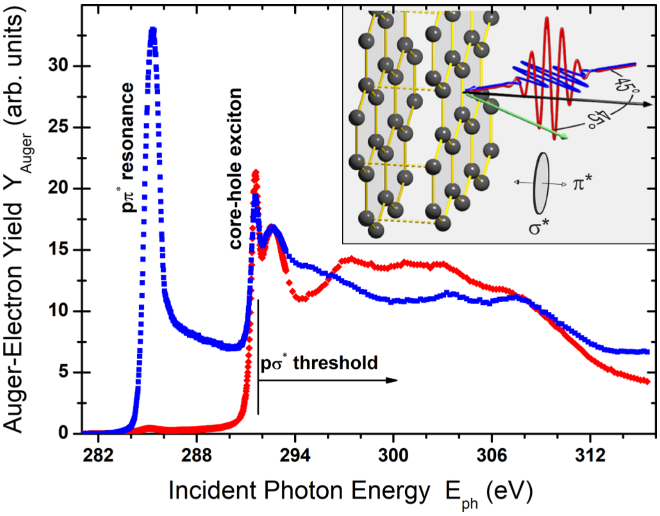

FIG. 6. NEXAFS spectra obtained from the *KVV*-Auger electron count rate normalized to the energy-dependent incident photon intensity ($\Theta_{tar} = 45^\circ$) and after subtraction of a small photoionization background due to valence bands. Both spectra are taken from the same HOPG crystal surface after cleaving and mild annealing. Squares (blue) are related to *p*-polarization and diamond symbols (red) stand for *s*-polarized x rays. The inset displays two HOPG surface layers (atom symbols in dark gray), incident x rays at a polar angle of 45° with two linear polarization directions (blue and red wave symbols) and the Auger-electron detection direction at 45° (green arrow). Furthermore, the spatial direction of the π^* orbital is depicted as small arrow, whereas the σ^* orbitals are confined within the orthogonal (basal) plane [6].

B. Static NEXAFS spectra

Figure 6 displays static NEXAFS spectra from HOPG for *s*- and *p* polarization at the carbon-*K* shell, taken at a photon-energy resolution of 43 meV [14]. In order to be most sensitive to structural details in the uppermost surface layer, the valence-electron background of <3% due to photoionization from deeper layers has been subtracted from the raw data using the measured peak shape of the valence-band photoionization. The NEXAFS spectra show several peak structures, and the dominant ones are due to excitation of the $p\pi^*$ resonance and superimposed eDOS maxima of different symmetry near the $p\sigma^*$ threshold (σ contribution ~30% [4]). Slightly below this threshold, at the energy of about 291.6 eV, the well-known peak due to core-hole excitons is visible as a narrow line in both spectra. For the linewidth we determine a FWHM of 0.47 eV, in accord with the literature value of 0.5 eV FWHM [8].

The inset in the figure illustrates the effect of polarization on the excitation probability of the $p\pi^*$ and $p\sigma^*$ resonances. As the $p\pi^*$ resonance in Fig. 6 is a separated peak without any admixture of different partial waves, we will focus on this specific peak at 285.3 eV. X rays with *p* polarization correspond to blue wave symbol indicating electric-field oscillations inside the scattering plane (see inset). Dependent on the polar angle Θ_{tar}, these incident x rays involve an electric-field vector component along the spatial π^* direction. The modulus square of the corresponding transition-matrix element is proportional to $I_{\pi^*}(\Theta_{tar}) \sim \sin^2(\Theta_{tar})$ and

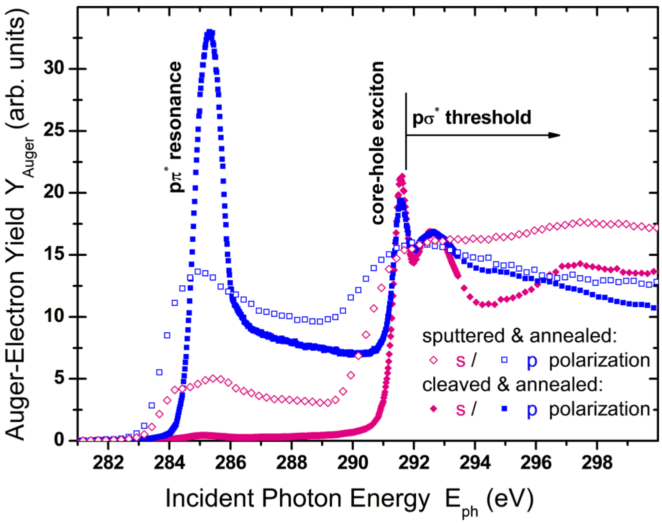

FIG. 7. Near-resonant absorption spectra (similar to Fig. 6) derived from the *KVV*-Auger electron count rate by normalization to the incident photon intensity (at $\Theta_{tar} = 45^\circ$) and after subtraction of a small photoionization background due to valence bands. Closed symbols stand for the crystalline HOPG surface (after cleaving) and open symbols represent the effect of damaged surface layers (amorphization due to low-energy Ar-ion irradiation). Squares (blue) are related to *p*-polarization and diamond symbols (pink) stand for *s*-polarized x rays.

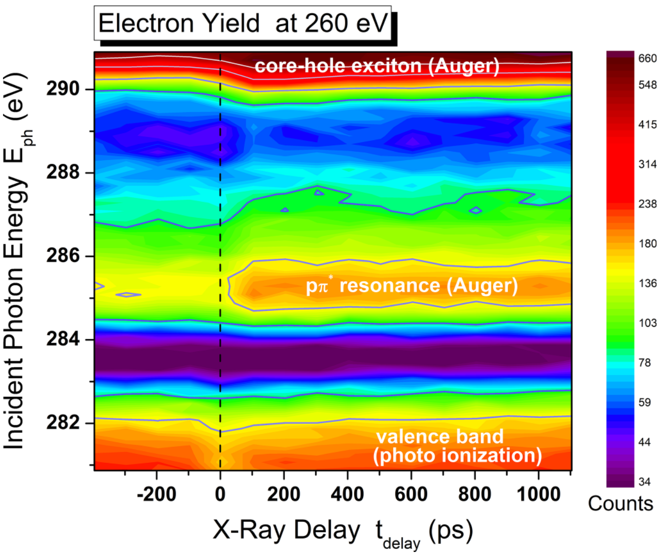

FIG. 8. Two-dimensional contour plot of the measured electron yield at the Auger maximum vs x-ray probe delay and photon energy. The plot includes 816 data points and has been taken during a continuous data acquisition over 5.5 h. These raw data have been obtained for a laser power of 1.9 W ($\phi_{in} = 146\,\mathrm{mJ/cm^2}$) and for *s*-polarized x-ray light at grazing incidence ($\Theta_{tar} = 70^\circ$). Clear effects due to the laser-induced excitation are visible at and beyond $t_{\rm delay} = 0$ (see text).

describes the excitation yield [5,6]. Contrary, an *s*-polarized x-ray beam involves no electric-field component in the $p\pi^*$ direction, and absorption as well as the resulting Auger yield are significantly suppressed. This theoretically expected strong dichroism of the $p\pi^*$ resonance is in very good agreement with our two spectra in Fig. 6, where we find a suppression by up to a factor of 70 for *s* polarization (red diamond symbols) compared to the *p*-polarization case (blue square symbols).

The spectra displayed in Fig. 6 have been obtained for HOPG after cleaving and moderate annealing for two x-ray polarization directions. These spectra correspond to atomically clean surfaces with a nearly flat crystalline structure. Exactly the same spectra are displayed also in Fig. 7 with solid symbols. For comparison to these crystalline HOPG results, spectra for the amorphized surface (after *in situ* irradiation of the HOPG sample with 3-keV Ar ions and subsequent mild annealing for outgassing of implanted Ar atoms) have also been taken. The amorphized surface (defect-rich on an atomic scale) leads to a strong and asymmetric smearing out of all peaks and also to some peak shifts. Under this condition, the core-hole excitonic peak vanishes even completely. Most striking, however, is the behavior of the $p\pi^*$ resonance yield. The corresponding ratio for *s*- over *p* polarization of the x rays (linear dichroism) is reduced from 70 to about 2.7 for the damaged surface layer. This shows that atomic disorder (related to the surface roughness) degrades the polarization sensitivity of the Auger yield significantly.

C. Dynamics under laser excitation

At this point, we were wondering whether nonresonant high-power laser irradiation is capable of influencing the $p\pi^*$ bond direction on short timescales, which we monitor via the resonant dichroic signal with nearest-neighbor bond-angle sensitivity. Before we present and discuss the corresponding pump-probe measurements, however, we try to shed some more light on the laser-induced excitation and equilibration processes in HOPG at our experimental conditions. As discussed in the section on laser-induced temperatures, the target was always kept clearly below its ablation threshold [20], and no indication of a permanent target modification or macroscopic temperature effects was observed (no modification of Auger or photoelectron spectra, no visible surface structuring at the laser spot, no pressure rise, no time variations of target current or electron signal). Regarding the electronic motion, we extract a peak electron temperature of $T_e^{\rm peak} = (5300 \pm 250)$ K, for a time period of $\tau_{\mathbf{e}} = 50$ to 200 fs consistent with literature values (see Sec. II B). This temperature is very small compared to the (extremely large) Fermi temperature of HOPG (≈200 000 K) and correspondingly the resulting populated band structure yields no significant deviations from its density of states times the Fermi-Dirac distribution, even at local electron temperatures up to 60 000 K [22]. The only known irregularity in graphite at slightly lower electron temperatures is a sudden drop of the electron transport cross section above 35 000 K [22]. A similar robustness of the band structure has also been found for other metals such as, e.g., Be, in strong contrast to the diatomic insulator BeO [39]. Thus, for our semimetallic graphite crystal, we expect no direct electronic effects inside the sample on timescales beyond a few 100 fs, where electron and lattice temperatures are in equilibrium.

Figure 8 is a color-coded two-dimensional time-resolved NEXAFS plot of the electron yield at the kinetic electron energy of about 260 eV as function of photon energy E_{ph} vs pump-probe delay. It shows three different spectral features: resonant core-hole excitonic Auger emission, resonant $p\pi^*$ Auger emission, and valence-band photoionization. More detailed, these features are (i) 1*s*-absorption structures in the Auger yield above $E_{ph} = 290$ eV due to final π^* states, σ^* states, and specifically core-hole excitons; (ii) *KVV*-Auger-electron emission for excitation of the $p\pi^*$ resonance at an excitation energy of 285.3 eV; and (iii) photoionization of valence-band electrons for a fixed final-state energy (with the fully populated $2s\sigma$ band [22] distributed around $E_{ph} = 279$ eV). Measurements have been performed at grazing incidence ($\Theta_{tar} = 70^\circ$) with *s*-polarized X-ray light and laser pulses of an energy of 0.31 mJ focused into a spot of about $0.8 \times 0.27\,\mathrm{mm}^2$ (horizontal × vertical) on the surface (incident fluence of $\phi_{in} = 146\,\mathrm{mJ/cm}^2$, absorbed fraction [19] of $\phi_{abs} = 42\,\mathrm{mJ/cm}^2$). It turned out that this relatively high-energy density, a factor of 3 below the ablation threshold [20], was necessary for achieving significant pump-probe effects and we did not observe any indications for modification of the surface quality even after long-lasting exposure.

It can be seen that photoionization features a 20% intensity drop at around $t = 0$, when the femtosecond laser is interacting with the target. Within a time duration of about 100 ps such an effect is expected, since space-charge acceleration [17] by slow laser-generated electrons shifts the valence-band photoelectrons (peak *V*-PI in Fig. 5) further beyond the selected kinetic electron-energy of 260 eV. Such a prompt suppression is not directly visible for the two Auger-decay structures in Fig. 8 since a kinetic-energy shift of about 2 eV leads only to intensity changes of a few percent for the chosen Auger-detection energy at the flat top of the peak (cf. inset Fig. 5). Contrary to such a short-time suppression, the Auger intensities of the core-hole exciton peak and of the $p\pi^*$-resonance excitation are rising significantly for $t > 0$. The $p\pi^*$ resonance involves an intensity enhancement by about 25%, pointing to a modified $p\pi^*$ bond direction, and there is an additional strong asymmetric broadening of the corresponding resonance spectrum. Despite additional features, we will focus in the following on the strength of this transition from the 1*s* state into the $p\pi^*$ resonance.

Figure 9 displays the delay-time dependence of the $p\pi^*$ resonance absorption for the two different directions (*s* and *p*) of linear x-ray polarization. The solid curves show least-square time-distribution fits including a convolution with a Gaussian resolution function represented by a root-mean-square width of $\sigma_{\mathrm{Gauss}} = (26 \pm 2)$ ps that agrees perfectly with the measured bunch length of the BESSY II electron-storage ring of (25.7 ± 1.5) ps (determined with a streak camera for the used hybrid bunch during our main experimental campaign). The fits are based on an exponential decay function with positive amplitude for *s*-polarized x rays and negative amplitude for *p*-polarization, respectively. This decay function is superimposed on a biased residual resonance yield and modified by a slightly asymmetric cusp-shaped function representing an intensity reduction due to space-charge shifts. The corresponding energy detuning is shown in Fig. 5 (inset) and leads to slightly reduced measured Auger-peak intensities and to the significant reduction of the photoionization yield in Fig. 8. The shape of this function has been extracted from previous space-charge investigations on Cu Auger and photoelectron lines [17] and is rescaled to the C-*KVV* Auger-electron speed (dashed curves in Fig. 9). Time zero is defined by the negative space-charge peak maximum without the bunch-length convolution [17]. Furthermore, a small time shift of the onset of the exponential decay function was allowed for in the fit.

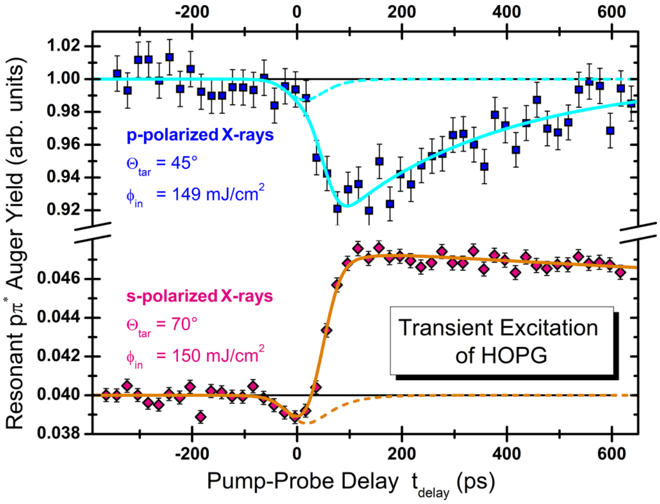

FIG. 9. Transient *KVV*-Auger intensity ($E_{kin} = 260\,\mathrm{eV}$) vs x-ray time delay with respect to the laser pulse, taken at the $p\pi^*$ resonance energy for fixed incident laser flux ϕ_{in}. Upper symbols (blue squares): measurements for a laser power of 0.94 W ($\phi_{in} = 149\,\mathrm{mJ/cm}^2$) using *p*-polarized x rays at 45°. Lower symbols (pink diamonds): near-grazing incidence measurements for a laser power of 1.96 W ($\phi_{in} = 150\,\mathrm{mJ/cm}^2$), but with *s*-polarized x rays. Pure data-acquisition time for both sum spectra was 3.5 h without the time for additional alignment checks and for the measurement of auxiliary data (e.g., target currents and detector noise) in between. Solid curves are fits to the data and are described in the text and the dashed curves indicate the (convoluted) contribution of space-charge acceleration.

The lower experimental dataset for *s*-polarized x rays is similar to a cut through the 2D distribution in Fig. 8 for the fixed excitation energy of 285.2 eV. In Fig. 9, however, a slightly larger power of the femtosecond pump laser has been used and 30 individual time spectra have been summed up (instead of only 3). It is clearly visible that the relative count rate is increasing by $(18.7 \pm 1)\%$ after the laser excitation at time t_0. Beyond about $t_{\mathrm{delay}} = 200$ ps it is relaxing slowly [a least-square fit results in an exponential decay time of $\Delta t_s = (4700 \pm 800)$ ps] towards the constant baseline at the yield of 0.040. Note that we found a similar steplike increase by $(16 \pm 5)\%$ as well as decay time for a few test spectra obtained at lower laser power (940 mW, $\phi_{in} = 150\,\mathrm{mJ/cm}^2$) for the target-tilt angle of $\Theta_{tar} = 45^\circ$. Thus, the pump effect seems to scale with ϕ_{in}, the laser energy density on the surface. The space-charge effect is consistent with a maximum Auger-energy shift of $\Delta E_{SC} = (4 \pm 1)$ eV for the lower curve in Fig. 9.

The upper experimental dataset has been obtained with *p*-polarized x-ray light for the same geometry as in Figs. 6

and 7 ($\Theta_{tar} = 45^\circ$). Note that 25 individual spectra have been summed up and the incident x-ray flux was significantly reduced for this case in order to avoid count-rate saturation effects. The time-dependent count rate is decreasing by about $(7.5 \pm 0.7)\%$ after t_0 and relaxes with a decay time of $\Delta t_p = (315 \pm 30)$ ps back to its undisturbed value. A space-charge shift ΔE_{SC} of the carbon *KVV*-Auger structure has directly been measured under similar conditions, using the method described previously [17] (see Fig. 5 inset). The corresponding intensity reduction of $\Delta I/I = (-1.3 \pm 0.6)\%$ is shown as (blue) dashed curve.

Probably the most striking observation from Fig. 9 is the laser-induced increase of the $p\pi^*$ resonance yield for *s*-polarized x rays, in contrast to the yield reduction for *p* polarization. Thus, the x-ray linear dichroism is significantly reduced after the laser pulse. Such a transient behavior points to *laser-induced dynamics of surface atoms*, which is probably dominated by atomic displacements of surface atoms along the *c* direction [37]. The relative effect is by far not as strong as the influence of static surface amorphization (see Fig. 7), but it shows the same trends. The asymmetric energy broadening of the $p\pi^*$ resonance (an extension towards higher photon energies) observed for the laser-induced profile of the line in Fig. 8 is also found for the defect-rich surface (even at both polarization directions in Fig. 7). Since electronic effects can be ruled out (see the discussion at the beginning of this section as well as Sec. II B), the subsequent interpretation of the $p\pi^*$ resonance excitation and decay will focus solely on lattice dynamics effects.

The thermal conductivity is extremely anisotropic with about $\kappa_{bp} = (1900 \pm 100)$ W/(K m) inside the HOPG basal plane in comparison to $\kappa_c = (8 \pm 1)$ W/(K m) along the principal axis *c* at room temperature and both values are nearly a factor of 2 lower at the estimated high lattice temperatures [40,22]. A survey of the lattice-heat relaxation channels indicates that the low thermal conductivity in the *c* direction determines the initial cooling time of about 7 ns from the surface to the cold bulk region beyond the depth of about 40 nm increased by an electron-diffusion distance of the same value. This estimated time agrees reasonably well with the experimental relaxation time of about 5 ns for the lower curve of Fig. 9. It does, however, significantly overestimate the relaxation time of the upper dataset for *p*-polarized x rays, which will be discussed at the end of this section.

Not only the thermal conductivity in graphite is anisotropic, but also the thermal expansion. At our maximum lattice temperatures, one expects an increase of the lattice *c* spacing by about 12% [41,42], whereas the variation in the basal plane is far below 1% (with a temperature-dependent sign) [41]. According to theory, the HOPG layer structure should lead to strong atomic out-of-plane oscillations at elevated temperatures [37] and such oscillations have also been found in recent experiments [33]. These oscillations break the crystal symmetry at the surface and explain the significant influence of the laser pulse on the resonant *KVV*-Auger yield, as seen in Figs. 8 and 9.

The speed of sound along the *c* axis in HOPG is 4140 m/s at room temperature [42] and 2300 m/s near the melting point [26]. This corresponds to a transport of a laser-generated sound wave to the absorption edge ins space (corrected for fast electron diffusion) and back to the surface within about 60 ps. This is also consistent with results of a 1D simulation describing a compressive strain wave leaving the HOPG surface in the bulk direction with additional signatures of multiple dynamic reflections inside the bulk (at delay periods of 40 to 60 ps) [42]. Such strain waves from deeper below the surface might trigger a correlated surface motion and amplify out-of-plane oscillations. This could be the reason why our fit for the *s*-polarized case in Fig. 9 yields a clear time difference Δt_{sh} of (50 ± 10) ps between the prompt space-charge suppression [17] and the onset of the Auger-intensity increase. For the upper curve (*s*-polarization) in Fig. 9, an accurate time shift cannot be extracted in a reliable way. A separate fit indicates a slightly smaller shift for this curve, but because of too-large statistical uncertainties we kept the delay of 50 ps also for this fit function. With this evidence for a time shift, one may check the 2D plot in Fig. 8 once again. In that plot, time zero is clearly marked by the intensity minimum of the valence-band photo ionization. An analysis shows that the center of the rising slope of the $p\pi^*$ resonance Auger yield is delayed by (55 ± 25) ps also in this dataset. These agreements between measured delays and computed reflection time suggests that delayed strain waves might trigger the resonant dichroic signal. It is, however, also conceivable that an accumulation of specific surface-vibration modes or of nucleation sites at the surface (similar to superheating) is responsible for the observed delay.

Finally, in connection to Fig. 9 we analyze intensity difference and relaxation-time variations for *p*-polarized vs *s*-polarized x rays. Strain waves and/or thermal motion are shaking the HOPG surface atoms in two independent directions [33,37,42]. This leads to transient local surface slopes parallel to the beam projection at angles $\varphi_p(t)$ and also perpendicular to the scattering plane at angles $\varphi_s(t)$ with respect to the basal plane. Such laser-induced slopes influence the resonant $p\pi^*$ excitation yield dependent on the linear polarization direction

(1) For an *s-polarized* x-ray beam, the electrical-field vector lies inside the basal plane, perpendicular to the projected light direction. Thus, there is no overlap with the $p\pi^*$ orbital direction and for a perfectly aligned and flat surface (no surface defects, no zero-point or thermal atomic displacements) the corresponding Auger yield is zero, as follows from dipole-matrix elements. A slope parallel to the beam projection does not influence the Auger yield (it stays zero), but any perpendicular slope at an angle φ_s leads to the well-known excitation yield [5,6] given by $I^{s\text{-}pol}_{p\pi^*}(\varphi_s) \sim \sin^2\varphi_s$.

(2) For a *p-polarized* x-ray beam one expects an excitation yield of the $p\pi^*$ resonance given by $I^{p\text{-}pol}_{p\pi^*}(\Theta_{tar} + \varphi_p, \varphi_s) \sim \cos^2\alpha$, with the squared angular mismatch $\alpha^2 = (\Theta_{tar} + \varphi_p - 90^\circ)^2 + \varphi_s^2$. At extreme grazing angles Θ_{tar} this expression simplifies strongly. Our setup, however, did not allow for choosing values of Θ_{tar} significantly beyond 70°.

Note that the above equations neglect electron-transport effects [43,44], but the corresponding influence on the results will be overshadowed by the dominant first-layer contribution of carbon *KVV*-Auger emission and sharp angular structures will be smeared out by the large detection solid angle of our

RBB spectrometer [16]. A simulation based on independent harmonic variations of local slopes in the s- and p directions using the above formulas with equal amplitudes $\varphi_s^{\max} = \varphi_p^{\max}$ yields the following results:

(1) A slope amplitude for the transvers direction is obtained from fitting the simulated normalized excitation growth $\Delta I_{p\pi^*}^{s\text{-}pol}/I_{p\pi^*}^{p\text{-}pol}$ to the experimental value for s-polarized x rays at 70° incidence. A mean value of $\varphi_s^{\max} = 6.6^\circ$ is obtained for the normalized experimental intensity rise of +0.75% in Fig. 9 (corresponding to $T_{\text{lattice}} \approx 3300$ K; see Table I).

(2) Using the above equation for $I_{p\pi^*}^{p\text{-}pol}$, the experimental intensity drop of −7.5% yields amplitudes $\varphi_s^{\max} = \varphi_p^{\max} \approx 20^\circ$ for p-polarized x rays at 45° incidence. These large slopes might be reasonable in the light of the estimated maximum bulk lattice temperature ($T_{\text{lattice}} \approx 4600$ K; see Table I) that is only slightly below the melting point of HOPG (see Fig. 3). They are roughly consistent with the Lindemann criterion [45] that yields a maximum atomic displacement of about 28% of the interatomic distance as a condition for melting. The corresponding maximum local angular-slope amplitude is 22 ° between neighboring atoms with uncorrelated displacements. This might be an indication for a possible phase transition at the surface.

(3) From our experimental ratio of *p- to s-polarization* $R_{p/s} = 2.7$ and both above formulas, we derive amplitudes $\varphi_s^{\max} = \varphi_p^{\max} \approx 33^\circ$ for the slopes of the surface due to amorphization by Ar ion irradiation at normal incidence (see Fig. 7). We assume that the assumption of harmonic slopes leads to enhanced uncertainties for this case. The very large slopes, however, confirm that the amorphized graphite surface is extremely rough, involving atomic surface steps.

The large, fitted slopes for the 45° incidence led us to a deeper investigation of the behavior of $I_{p\pi^*}^{p\text{-}pol}$ at different polar angles Θ_{tar}. During this analysis, we were caught by surprise that our reference configuration with $\Theta_{tar} = 45^\circ$ is a very special case regarding the slope sensitivity for p polarization. Under these conditions, the positive- and negative half waves of φ_p cancel each other completely and the drop of the $p\pi^*$ resonance intensity is given mainly by $\varphi_s^{\max}$ (plus a small cross term). It is important to realize that each of the half waves of φ_p alone leads to an intensity drop or intensity rise exceeding the effect of $\varphi_s^{\max}$ by about one order of magnitude (and even more for smaller angular amplitudes). Hence, if one of these half waves is changed by only a few percent, the intensity drop might change completely. We are confident that a small perturbation such as an inharmonic potential contribution along φ_p or strain fields at the surface with directional components in the basal plane can significantly change the dichroic x-ray response. Specifically at an incident angle of 45°, this can influence the magnitude of the intensity drop and maybe also the decay time of the $p\pi^*$ resonance signal measured with p-polarized x rays.

IV. CONCUSIONS AND OUTLOOK

In summary, we have investigated the short-time reaction of highly oriented pyrolytic graphite induced by femtosecond-laser pulses in a series of laser-pump–x-ray-probe experiments. For this sake, time-resolved near-edge x-ray absorption is employed as a surface-sensitive probe to study the dynamics of surface distortion by atomic motion in HOPG upon laser excitation. Auger-electron detection is used to probe an ultrafast surface distortion, by monitoring the *KVV*-Auger electron signal of the $p\pi^*$ resonance absorption with nearest-neighbor bond-angle sensitivity relative to the linear x-ray polarization vector. This is a short-time dynamics study of the polarization dependence of near-edge K-shell resonances of HOPG.

Technically innovative are the large detection solid angle and an energy window optimized for Auger measurements of the RBB electron spectrometer as well as its effective suppression of scattered laser light and laser-induced secondary electrons. Preparative HOPG electron spectroscopy data for nonresonant as well as resonant carbon K-shell excitation without laser pump pulses as function of the angle of incidence and of the linear polarization direction are in very good agreement with previous data. The same holds true for angular-dependent TEYs and NEXAFS spectra. The measured narrow core-hole exciton line indicates a good quality of the sample and of the experimental setup. Measured absolute total electron yields and manyfold of consistent literature values on the properties of HOPG enable a determination of characteristic electron temperatures and lattice temperatures due to the laser irradiation. Thus, the basic experimental boundary conditions for a target at room temperature as well as for the laser interaction with HOPG are well under control.

The auxiliary experiments mentioned above have paved the way for meaningful investigations of resonant carbon K excitations into unpopulated states using nonresonant high-power laser pulses as a 100-fs pump signal acting significantly on the surface atomic structure. We also can conclude that electron-dynamics effects will have no significant influence on the interpretation of the resonance data on a picosecond timescale. Beyond the expected space-charge acceleration of Auger electrons and of photoelectrons from the $2s\sigma$ band, we find clear laser-induced transient modifications of width and intensity of different spectral features (Auger decay of the core-hole exciton, of the $p\pi^*$ resonance state, and of the mixed peak above the $p\sigma^*$ resonance threshold) that relate to modifications of the atomic lattice structure. Specifically for the $p\pi^*$ resonance absorption by K-shell electrons involving a simple polarization dependence [5,6], the laser pulse introduces a clear dichroic signal, namely an enhanced intensity for s-polarized x rays and a reduction for p-polarized x rays. These reactions are delayed by about 50 ps with respect to the laser pulse and an asymmetric resonance line broadening is observed as well. In comparison to results for an amorphized carbon surface (produced *in situ* from HOPG), the findings for crystalline HOPG point to a high sensitivity regarding laser-induced deviations from the planar-surface geometry.

The combination of polarization sensitivity and Auger-electron detection used in this work sheds light on correlated short-time vibrations of surface atoms employing the Auger emission as an alternative probe channel for structural changes, as it is element- and bond selective restricted to the uppermost surface layers by the small electron-escape depth. Quantitative information on the amplitude of local surface slopes is extracted from Auger-yield simulations for the influence of 2D tilt angles on the excitation by linearly polarized x-ray beams. These simulations yield mean perpendicular angular slopes that agree with the tendency of the estimated laser-induced lattice temperatures. For the experiment with *s*-polarized x rays at the grazing-incidence angle of 70°, also the relaxation time of 4.7 ns of the transient resonance excitation is well described by diffusive heat transport into the bulk of the sample.

However, a significantly shorter relaxation within 315 ps is found for *p*-polarized x rays at an incident angle of 45°. The corresponding Auger-yield simulations have revealed that this combination of incident angle and polarization direction involves an unexpected high sensitivity to small nonlinearities, which might have a strong influence on the relaxation time. This interpretation could be checked by a similar measurement with *p*-polarized x rays at 70°, but with a strong additional reduction of the x-ray flux for avoiding count-rate saturation effects. In future investigations, the specific sensitivity at 45° might be used in combination with more advanced theoretical methods [46] to get access to details of correlated atomic motions and to strain fields at the surface. It should be mentioned, however, that the angular slopes for the 45° case in this work are so close to the Lindemann melting criterion [45] that we cannot completely exclude a transient and local melting at the surface which would influence the relaxation. From the theoretical point of view, the validity and precision of the Lindemann criterion is even nowadays, more than 100 years after its publication, still a matter of controversy [47,48]. Experimentally, such local surface-melting effects should vanish completely if the laser power would be reduced by 20 to 30%.

For a deeper understanding of the delayed initial reaction of the x-ray signal, one might investigate whether it relates to strain waves and possibly strain-wave reflections inside the laser-heated volume or whether it is a collective effect like superheating at temperatures close to a phase transition. The first effect could be verified by changing the effective excitation depth via variation of the laser wavelength or by using a structured target with a thin graphitic top layer. The second effect could be checked by a variation of the transient lattice temperature via the laser power. The temperature-dependent number of nucleation sites should have a significant effect on superheating delay. The determination of the spatial range of the surface slopes (Brownian motion of individual atoms vs specific phonons at long wavelength vs strain fields) might call for supporting measurements at grazing-incidence angles (x-ray diffraction [18], electron diffraction or proton scattering).

ACKNOWLEDGMENTS

We are indebted to N. Pontius for his comments on the manuscript, and to the BESSY II crew and to T. Blume for their important help during the experimental phase. The ET setup was nearly exclusively financed by the Helmholtz-Strategy Fund “Ion Tracks In Solids” (2000).

[1] J. E. Houston, J. W. Rogers Jr., R. R. Rye, F. L. Hutson, and D. E. Ramaker, Relationship between the Auger line shape and the electronic properties of graphite, Phys. Rev. B **34**, 1215 (1986).

[2] G. S. Painter and D. E. Ellis, X-ray photoemission studies of diamond, graphite, and glassy carbon valence bands, Phys. Rev. B **1**, 4747 (1970).

[3] A. Zunger, Self-consistent LCAO calculation of the electronic properties of graphite - I. The regular graphite lattice, Phys. Rev. B **17**, 626 (1978).

[4] R. Ahuja, S. Auluck, J. Trygg, J. M. Wills, O. Eriksson, and B. Johansson, Electronic structure of graphite: Effect of hydrostatic pressure, Phys. Rev. B **51**, 4813 (1995); see references quoted therein.

[5] R. A. Rosenberg, P. J. Love, and V. Rehn, Polarization-dependent C(K) near-edge x-ray-absorption fine structure of graphite, Phys. Rev. B **33**, 4034 (1986).

[6] J. Stöhr, *NEXAFS Spectroscopy*, edited by G. Ertl, R. Gomer, and D. L. Mills (Springer, Berlin, 1996).

[7] D. A. Fischer, R. M. Wentzcovitch, R. G. Carr, A. Continenza, and A. J. Freeman, Graphitic interlayer states: A carbon K near-edge x-ray-absorption fine-structure study, Phys. Rev. B **44**, 1427 (1991).

[8] Y. Ma, P. Skytt, N. Wassdahl, P. Glans, D. C. Mancini, J. Guo, and J. Nordgren, Core Excitons and Vibronic Coupling in Diamond and Graphite, Phys. Rev. Lett. **71**, 3725 (1993). P. Skytt, P. Glans, D. C. Mancini, J.-H. Guo, N. Wassdahl, and J. Nordgren, and Y. Ma, Angle-resolved soft-x-ray fluorescence and absorption study of graphite, Phys. Rev. B **50**, 10457 (1994).

[9] G. Schiwietz, G. Xiao, P. L. Grande, E. Luderer, R. Pazirandeh, and U. Stettner, Determination of the electron temperature in the thermal spike of amorphous carbon, Europhys. Lett. **47**, 384 (1999).

[10] E. Gruber, R. A. Wilhelm, R. Pétuya, V. Smejkal, R. Kozubek, A. Hierzenberger, B. C. Bayer, I. Aldazabal, A. K. Kazansky, F. Libisch *et al.*, Ultrafast electronic response of graphene to a strong and localized electric field, Nat. Commun. **7**, 13948 (2016).

[11] C. D. Spataru, M. A. Cazalilla, A. Rubio, L. X. Benedict, P. M. Echenique, and S. G. Louie, Anomalous Quasiparticle Lifetime in Graphite: Band Structure Effects, Phys. Rev. Lett. **87**, 246405 (2001).

[12] G. Moos, C. Gahl, R. Fasel, M. Wolf, and T. Hertel, Anisotropy of Quasiparticle Lifetimes and the Role of Disorder in Graphite from Ultrafast Time-Resolved Photoemission Spectroscopy, Phys. Rev. Lett. **87**, 267402 (2001).

[13] S. Tan, A. Argondizzo, C. Wang, X. Cui, and H. Petek,, Ultrafast Multiphoton Thermionic Photoemission from Graphite, Phys. Rev. X **7**, 011004 (2017); see references quoted therein.

[14] G. Schiwietz, M. Beye, and T. Kachel, UE112_PGM-1: An open-port low-energy beamline at the BESSY II undulator UE112, J. Large-Scale Res. Facil. **1**, A33 (2015).

[15] K. J. S. Sawhney, F. Senf, M. Scheer, F. Schäfers, J. Bahrdt, A. Gaupp, and W. Gudat, A novel undulator-based PGM beamline for circularly polarised synchrotron radiation at BESSY II, NIM A **390**, 395 (1997); see also https://www.helmholtz-berlin.de/pubbin/igama_output?modus=einzel&gid=1642.

[16] G. Schiwietz, M. Beye, D. Kühn, and G. Xiao, The retarding Bessel Box—An electron spectrometer designed for

pump/probe experiments, J. Electron Spectrosc. Relat. Phenom. **203**, 51 (2015).

[17] G. Schiwietz, D. Kühn, A. Föhlisch, K. Holldack, T. Kachel, and N. Pontius, Laser-pump/X-ray-probe experiments with electrons ejected from a Cu (111) target: Space-charge acceleration, J. Synchrotron Radiat. **23**, 1158 (2016); Dynamics of space-charge acceleration of x-ray generated electrons emitted from a metal surface, J. Electron Spectrosc. Relat. Phenom. **220**, 40 (2017).

[18] K. Sokolowski-Tinten, C. Blome, J. Blums, A. Cavalleri, C. Dietrich, A. Tarasevitch, I. Uschmann, E. Förster, M. Kammler, M. Horn-von-Hoegen, and D. von der Linde, Femtosecond X-ray measurement of coherent lattice vibrations near the Lindemann stability limit, Nature **422**, 287 (2003).

[19] Data are obtained from the database and evaluation code by M. Polyanskiy at https://refractiveindex.info/. Computations have been averaged over internal data sets for graphite by Djurišic and Li (1999) as well as for HOPG by Song, Gu, Zhu, Jiang, Chen, Zhang, Liu (2018).

[20] K. Sokolowski-Tinten, S. Kudryashov, V. Temnov, J. Bialkowski, D. von der Linde, A. Cavalleri, H. O. Jeschke, M. E. Garcia, and K. H. Bennemann, *Femtosecond Laser-Induced Ablation of Graphite*, Ultrafast Phenomena XII, Springer Series in Chemical Physics, Vol. 66 (Springer, Berlin, 2001), pp. 425–427.

[21] C. J. Powell and A. Jablonski, NIST Standard Ref. Database **71**, NIST Electron Inelastic-Mean-Free-Path Database Version 1.1, (2000), http://dx.doi.org/10.18434/T48C78.

[22] G. Schiwietz, G. Xiao, E. Luderer, and P. L. Grande, Auger electrons from ion tracks, Nucl. Instrum. Methods Phys. Res., Sect. B **164-165**, 353 (2000), and references therein.

[23] A. Cezairliyan and A. P. Müller, Heat capacity and electrical resistivity of POCO AXM-5Q1 graphite in the range 1500–3000 K by a pulse-heating technique, Int. J. Thermophys. **6**, 285 (1985).

[24] V. N. Korobenko, A. I. Savvatimski, and R. Cheret, Graphite melting and properties of liquid carbon, Int. J. Thermophys. **20**, 1247 (1999).

[25] S. Picard, D. T. Burns, and P. Roger, Determination of the specific heat capacity of a graphite sample using absolute and differential methods, Metrologia **44**, 294 (2007).

[26] A. M. Kondratyev and A. D. Rakhel, Melting Line of Graphite, Phys. Rev. Lett. **122**, 175702 (2019), and references therein.

[27] S. Dusari, J. Barzola-Quiquia, P. Esquinazi, and N. García, Ballistic transport at room temperature in micrometer-size graphite flakes, Phys. Rev. B **83**, 125402 (2011).

[28] Z. G. Wang, C. Dufour, E. Paumier, and M. Toulemonde, The Se sensitivity of metals under swift-heavy-ion irradiation: A transient thermal process, J. Phys. **6**, 6733 (1994). See also references herein.

[29] B. Rethfeld, K. Sokolowski-Tinten, D. von der Linde, and S. I. Anisimov, Timescales in the response of materials to femtosecond laser excitation, Appl. Phys. A **79**, 767 (2004).

[30] N. W. Ashcroft and N. D. Mermin: *Solid State Physics* (Saunders College Publishing, New York, 1976), pp. 362–364.

[31] J. F. Ready, Mechanism of electron emission produced by a giant-pulse laser, Phys. Rev. **137**, A620 (1965).

[32] A. Stange, C. Sohrt, L. X. Yang, G. Rohde, K. Janssen, P. Hein, L.-P. Oloff, K. Hanff, K. Rossnagel, and M. Bauer, Hot electron cooling in graphite: Supercollision versus hot phonon decay, Phys. Rev. B **92**, 184303 (2015), and references therein.

[33] R. P. Chatelain, V. R. Morrison, B. L. M. Klarenaar, and B. J. Siwick, Coherent and Incoherent Electron-Phonon Coupling in Graphite Observed with Radio-Frequency Compressed Ultrafast Electron Diffraction, Phys. Rev. Lett. **113**, 235502 (2014).

[34] F. Carbone, G. Aubock, A. Cannizzo, F. Van Mourik, R. R. Nair, A. K. Geim, K. S. Novoselov, and M. Chergui, Femtosecond Carrier Dynamics in Bulk Graphite and Graphene Paper, Chem. Phys. Lett. **504**, 37 (2011).

[35] M. Breusing, C. Ropers, and Th. Elsaesser, Ultrafast Carrier Dynamics in Graphite, Phys. Rev. Lett. **102**, 086809 (2009).

[36] Y. Ishida, T. Togashi, K. Yamamoto, M. Tanaka, T. Taniuchi, T. Kiss, M. Nakajima, T. Suemoto, and S. Shin, Non-thermal hot electrons ultrafastly generating hot optical phonons in graphite, Sci. Rep. **1**, 64 (2011).

[37] K. H. Bennemann, Ultrafast dynamics in solids, J. Phys.: Condens. Matter **16**, R995 (2004), see references therein and Fig. 42.

[38] G. Schiwietz, J. P. Biersack, D. Schneider, N. Stolterfoht, D. Fink, V. J. Montemayor, and B. Skogvall, Investigation of δ-electron emission in collisions of highly charged fast Ne projectiles with carbon-foil targets, Phys. Rev. B **41**, 6262 (1990).

[39] G. Schiwietz, K. Czerski, M. Roth, P. L. Grande, V. Koteski, and F. Staufenbiel, Evidence for an Ultrafast Breakdown of the BeO Band Structure due to Swift Argon and Xenon Ions, Phys. Rev. Lett. **105**, 187603 (2010). See also references therein.

[40] A. A. Balandin, Thermal properties of graphene and nanostructured carbon materials, Nat. Mater. **10**, 569 (2011), and references therein.

[41] B. Marsden, A. Mummery, and P. Mummery, Modelling the coefficient of thermal expansion in graphite crystals: Implications of lattice strain due to irradiation and pressure, Proc. R. Soc. A **474**, 20180075 (2018).

[42] X. Wang, A. Jarnac, J. C. Ekström, A. U. J. Bengtsson, F. Dorchies, H. Enquist, A. Jurgilaitis, M. N. Pedersen, C.-M. Tu, M. Wulff, and J. Larsson, Generation of a large compressive strain wave in graphite by ultrashort-pulse laser irradiation, Struct. Dyn. **6**, 024501 (2019).

[43] M. Rösler and W. Brauer, *Particle Induced Electron Emission I*, Springer Tracts of Modern Physics, Vol. 122 (Springer, Berlin, 1991).

[44] F. J. García de Abajo, M. A. Van Hove, and C. S. Fadley, Multiple scattering of electrons in solids and molecules: A cluster-model approach, Phys. Rev. B **63**, 075404 (2001).

[45] F. A. Lindemann, Über die Berechnung molekularer Eigenfrequenzen, Physikalische Zeitschrift **11**, 609 (1910).

[46] R. Car and M. Parrinello, Unified Approach for Molecular Dynamics and Density-Functional Theory, Phys. Rev. Lett. **55**, 2471 (1985).

[47] M. M. Vopson, N. Rogers, and I. Hepburn, The generalized Lindemann melting coefficient, Solid State Commun. **318**, 113977 (2020).

[48] X. Fan, D. Pan, and M. Li, Rethinking Lindemann criterion: A molecular dynamics simulation of surface mediated melting, Acta Mater. **193**, 280 (2020).